



AFRL-RX-WP-TM-2010-4007

ADVANCED ENERGY STORAGE AND CONVERSION DEVICES

Michael F. Durstock

**Nanostructured and Biological Materials Branch
Nonmetallic Materials Division**

**DECEMBER 2008
Interim Report**

Approved for public release; distribution unlimited.

See additional restrictions described on inside pages

STINFO COPY

**AIR FORCE RESEARCH LABORATORY
MATERIALS AND MANUFACTURING DIRECTORATE
WRIGHT-PATTERSON AIR FORCE BASE, OH 45433-7750
AIR FORCE MATERIEL COMMAND
UNITED STATES AIR FORCE**

NOTICE AND SIGNATURE PAGE

Using Government drawings, specifications, or other data included in this document for any purpose other than Government procurement does not in any way obligate the U.S. Government. The fact that the Government formulated or supplied the drawings, specifications, or other data does not license the holder or any other person or corporation; or convey any rights or permission to manufacture, use, or sell any patented invention that may relate to them.

This report was cleared for public release by the Wright-Patterson Public Affairs Office and is available to the general public, including foreign nationals. Copies may be obtained from the Defense Technical Information Center (DTIC) (<http://www.dtic.mil>).

AFRL-RX-WP-TM-2010-4007 HAS BEEN REVIEWED AND IS APPROVED FOR PUBLICATION IN ACCORDANCE WITH ASSIGNED DISTRIBUTION STATEMENT.

*//Signature//

PATRICK S. CARLIN
Program Manager, Electrochemical Energy
Nanostructured and Biological Materials
Branch
Nonmetallic Materials Division

//Signature//

KRISTEN M. KEARNS, Chief
Nanostructured and Biological Materials
Branch
Nonmetallic Materials Division

This report is published in the interest of scientific and technical information exchange, and its publication does not constitute the Government's approval or disapproval of its ideas or findings.

*Disseminated copies will show “//Signature//” stamped or typed above the signature blocks.

REPORT DOCUMENTATION PAGE					<i>Form Approved</i> OMB No. 0704-0188	
The public reporting burden for this collection of information is estimated to average 1 hour per response, including the time for reviewing instructions, existing data sources, gathering and maintaining the data needed, and completing and reviewing the collection of information. Send comments regarding this burden estimate or any other aspect of this collection of information, including suggestions for reducing this burden, to Department of Defense, Washington Headquarters Services, Directorate for Information Operations and Reports (0704-0188), 1215 Jefferson Davis Highway, Suite 1204, Arlington, VA 22202-4302. Respondents should be aware that notwithstanding any other provision of law, no person shall be subject to any penalty for failing to comply with a collection of information if it does not display a currently valid OMB control number. PLEASE DO NOT RETURN YOUR FORM TO THE ABOVE ADDRESS.						
1. REPORT DATE (DD-MM-YY) December 2008			2. REPORT TYPE Interim		3. DATES COVERED (From - To) 01 October 2007 – 01 October 2008	
4. TITLE AND SUBTITLE ADVANCED ENERGY STORAGE AND CONVERSION DEVICES					5a. CONTRACT NUMBER IN HOUSE	
					5b. GRANT NUMBER	
					5c. PROGRAM ELEMENT NUMBER 61102F	
6. AUTHOR(S) Michael F. Durstock					5d. PROJECT NUMBER 4347	
					5e. TASK NUMBER 12	
					5f. WORK UNIT NUMBER 12200002	
7. PERFORMING ORGANIZATION NAME(S) AND ADDRESS(ES) Nanostructured and Biological Materials Branch (AFRL/RXBN) Nonmetallic Materials Division Air Force Research Laboratory, Materials and Manufacturing Directorate Wright-Patterson Air Force Base, OH 45433-7750 Air Force Materiel Command, United States Air Force					8. PERFORMING ORGANIZATION REPORT NUMBER AFRL-RX-WP-TM-2010-4007	
9. SPONSORING/MONITORING AGENCY NAME(S) AND ADDRESS(ES) Air Force Research Laboratory Materials and Manufacturing Directorate Wright-Patterson Air Force Base, OH 45433-7750 Air Force Materiel Command United States Air Force					10. SPONSORING/MONITORING AGENCY ACRONYM(S) AFRL/RXBN	
					11. SPONSORING/MONITORING AGENCY REPORT NUMBER(S) AFRL-RX-WP-TM-2010-4007	
12. DISTRIBUTION/AVAILABILITY STATEMENT Approved for public release; distribution unlimited.						
13. SUPPLEMENTARY NOTES PAO case number 88 ABW-2009-0779, cleared 27 February 2009. Report contains color.						
14. ABSTRACT This focuses on addressing the materials challenges posed in developing higher energy and power density batteries as well as in developing alternative fuel cell membrane materials.						
15. SUBJECT TERMS						
16. SECURITY CLASSIFICATION OF:			17. LIMITATION OF ABSTRACT: SAR	18. NUMBER OF PAGES 30	19a. NAME OF RESPONSIBLE PERSON (Monitor) Patrick S. Carlin	
a. REPORT Unclassified	b. ABSTRACT Unclassified	c. THIS PAGE Unclassified			19b. TELEPHONE NUMBER (Include Area Code) N/A	

LABORATORY ANNUAL TASK REPORT

LRIR #: 07ML05COR

Title: Advanced Energy Storage and Conversion Devices

Laboratory Task Manager:

Dr. Michael Durstock (AFRL/RXBN, DSN 785-9208), Michael.Durstock@wpafb.af.mil

AFOSR Program Manager:

Dr. Charles Lee (AFOSR/NL 703-696-7779)

Research Objectives:

This task focuses on addressing the materials challenges posed in developing higher energy and power density batteries as well as in developing alternative fuel cell membrane materials. The primary focus for thin film batteries centers on developing an understanding of the influence that the morphology and nanostructure of battery electrodes has on device performance (energy density, rate capability, stability, reversibility etc.). By developing alternative nanostructured electrode materials, higher Q_{rev} values, greater cyclability, and improved reversibility can be achieved. In order to accomplish this, precise control of the materials morphology is essential, which is a focus of this task. Carbon nanotubes and nanofibers can be synthesized in a variety of different methods and in a variety of different forms, all of which significantly influences their structure, morphology, and level of disorder which will, in turn, play an extremely significant role the lithium-ion intercalation process. This task addressed these issues by investigating and probing the influence that carbon nanostructure has on thin film battery device performance. In addition, alternative materials structures for fuel cell membranes are being investigated. Current materials (i.e. Nafion) used for proton exchange membranes in fuel cells are limited both in terms of operating temperature and in their requirement for relatively high humidities. This task addresses these restrictions by exploring alternative polymer materials that could be utilized for higher performance fuel cell systems.

Summary of Progress and Forecast for Next FY:

Employing nanoscale morphologies in battery electrode materials has been seen to greatly improve storage capacity and rate capability, two critical properties needing improvement to keep pace with the ever increasing power requirements of new technologies. However, the ability to control the morphology and to understand how it affects electrochemical behavior is the most critical component in developing new electrode materials which can solve current battery technology limitations, namely those dealing with size and weight. VAMWNT-Ni electrodes examined in this work showed highly reversible capacities that were almost twice graphite's maximum theoretical capacity. The VAMWNT-Ni also showed excellent rate capability up to currents not typically utilized in laboratory scale electrode testing. The improvement in these electrochemical properties is thought to be primary a result from the aligned nature of the MWNTs in the direction of battery cell current flow. In addition, new structures of matter have been designed and synthesized for use as proton exchange membranes in hydrogen-based fuel cells. Polymers based on sulfonated aryleneethioethersulfone (SPTES) have (previously) exhibited performance (conductivity) significantly higher than that observed in commercially available systems (Nafion). Ongoing efforts aimed at retaining good mechanical properties under stringent operating conditions of elevated temperature and humidity are discussed.

Use of Funds (FY08, \$K):

<u>In-house</u>	<u>Capital Equipment</u>	<u>On-Site Contractor</u>	<u>Contracts/Grants</u>
\$75	0	\$200	0

Funding Profile (\$K):

Reporting FY
\$275

Advanced Energy Storage and Conversion Devices

1. Overview:

The Air Force operates an extensive range of technologies which have vastly different power requirements. These technologies range from small portable electronic devices and unmanned aerial vehicles to military shelters and satellites. The diversity of technologies has created a need for varied forms of power generation and the ability to store power. The primary limitations of current power systems are their size and mass to power ratio, and the overall cost associated with integrating these systems into various technology platforms. This has led to an increased interest in the development of the materials and processing capabilities necessary to enable high-performance, next-generation power systems that are lightweight, flexible, and low-cost.

Specific approaches being pursued center on creating the ability to create low-cost, lightweight and potentially flexible power generation and energy storage systems. In order to enable these applications, a variety of components will be required and this task specifically focuses on addressing the materials issues faced by fuel cell membrane materials and thin film batteries, as detailed in this report. Applications of these technologies will include power generation and storage for unmanned aerial vehicles, next generation satellites, high altitude airships, a reduction in logistical burdens for airbase deployment, and a portable and renewable source of power for in theatre special operations personnel.

2. Nanostructured Batteries

2.1 Background and Objectives

Batteries are one of the most heavily utilized portable energy sources used in the Air Force today, from warfighters' electronic equipment to orbiting satellites. Limitations to current battery systems are primarily related to their size and mass to power ratio have increased interest in the development of the materials and processing capabilities necessary to enable high-performance, next-generation battery systems that can deliver the required power while being lightweight, flexible, and low-cost. New battery technologies must employ innovative electrode materials able to increase storage capacity and allow for higher rate capabilities, while maintaining high cyclability. Nanostructured electrode materials offer a solution to this problem because of their greatly increased surface area compared to conventional flat plate electrodes. The increased surface area allows for two fundamental improvements: 1) higher lithium uptake leading to increased storage capacity and 2) increased rate capability allowed through much faster interfacial kinetics.¹ This research focuses on understanding the relationship between electrochemical behavior and nanoscale morphological control of lithium-ion battery electrode materials, specifically looking at carbon-based electrode materials. In addition to the many available carbon morphologies they possess several other advantages, such as good electrical conductivity, lightweight, and dimensional and mechanical stability during lithium insertion and de-insertion, making them practical intercalation electrode materials. Figure 1 shows the capacity of various types of carbon battery electrodes. Region 1 includes graphitizable carbons, which despite their lower capacities have the best cyclability, as opposed to the hard and soft carbons of region 2 and 3, which have high initial capacities but very poor cyclability due to their structural properties. Region 4 includes various types of carbon nanotubes (CNTs) and carbon nanofibers (CNFs). These morphologies of carbon can exhibit very high capacities and great cyclability,

¹ Sadoway, D.R.; Mayes, A.M. *MRS Bulletin* 2002, 590.

however, research is needed to better understand these materials from a battery electrode perspective.

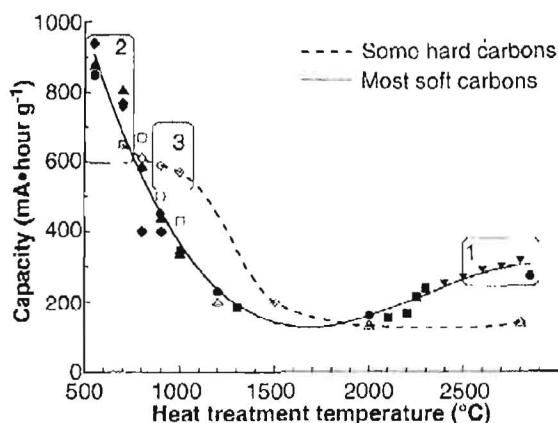


Figure 1 - Capacity as a function of heat treatment temperature for various types of carbon [modified from 8b]. Region 1 includes graphitizable carbons, while regions 2 and 3 include hard and soft carbons. Various CNTs and CNFs are included in Region 4.

2.2 Research Results

For the reasons we discussed regarding the importance of nanoscale morphological control over electrode materials we have focused on electrodes with two different morphologies. The first types of electrode are vertically aligned multi-walled carbon nanotubes (VAMWNTs) which are supported at their base by a metal film. The alignment of multi-walled carbon nanotubes (MWNTs) in the direction of current flow in a battery cell significantly increases the accessibility of lithium-ions to the interstitial spaces and internal tube structure of the MWNTs. Consequently, the specific capacity, reversibility, and cyclability of a battery cell can be significantly improved. Initially, the VAMWNTs were supported by a gold film (VAMWNT-Au); however, X-ray diffraction data indicated that lithium-ions were participating in an electrochemical alloying/de-alloying reaction with the gold, as well as, lithium-ion insertion into the VAMWNTs confirmed by Raman

spectral data. In order to isolate the electrochemical behavior of the VAMWNTs with lithium, a non-lithium alloying metal, nickel, was utilized as the support film at the base of the VAMWNTs (VAMWNT-Ni). Non-aligned multi-walled carbon nanotubes (MWNTs) and single-walled carbon nanotubes (SWNTs) comprised the second type of electrode materials, which were not aligned in the direction of current flow.

Various characterization methods were used to analyze electrochemical behavior (specific capacity, rate capability, and cyclability) and morphology of these electrodes in order to relate how they structurally change during electrochemical processes. Electrochemical characterization was carried out at room temperature in an argon filled glove box (H_2O and O_2 limit < 1 ppm) with a two-electrode cell. Lithium metal foil (Aldrich) was used as the counter electrode. The electrodes were separated by a Celgard® 2400 battery membrane soaked in a liquid electrolyte solution, consisting of 1.0 M lithium tetrafluoroborate (LiBF_4) in ethylene carbonate (EC)/diethyl carbonate (DEC) (1:1 v/v ratio) (Aldrich) solution. The electrochemical measurements were performed galvanostatically with voltage limits of 0.02

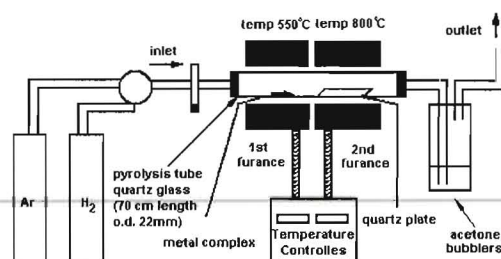


Figure 2 - Equipment set-up for the pyrolysis of iron phthalocyanine.

and 3.6 V vs. Li/Li^+ at various specific currents. Morphology of the electrodes was evaluated using a FEI Quanta scanning electron microscope (SEM) with energy dispersive X-ray spectroscopy (EDS) capabilities. Additionally, X-ray diffraction XRD patterns were recorded using a Bruker AXS D8 Discover spectrometer in transmission mode and

Raman spectroscopy was done on a Renishaw plc inVia Raman microscope.

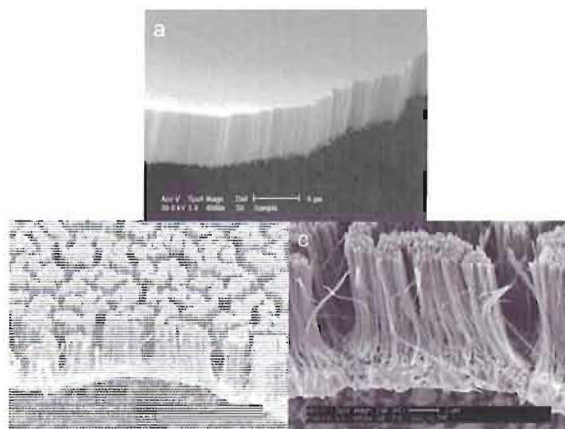


Figure 3 - SEM images of an a) free standing VAMWNTs (scale bar = 5 μm) and b) (scale bar = 10 μm) and c) VAMWNTs on a gold substrate (scale bar = 2 μm).

The VAMWNTs were synthesized via the pyrolysis of iron(II) phthalocyanine (FePc) under $\text{Ar}_{(\text{g})}/\text{H}_{2(\text{g})}$ at 800–1100° C on a quartz substrate according to published procedures using the set-up shown in Figure 2.² The FePc was introduced into the reaction chamber in the vapor phase where, upon thermal treatment the VAMWNTs grew from a quartz substrate. A 1–3 μm thick gold or nickel film was then sputtered onto the top surface of the VAMWNTs, which was then treated with a hydrofluoric acid solution in order to remove the quartz substrate. Figure 3 shows scanning electron micrographs of an 10.0 ± 0.3 μm tall VAMWNT mat with an average diameter of ~ 75 nm film post-synthesis (Figure 3a) and after transfer to a 1.0 ± 0.1 μm gold film (Figures 3b and c). The bunching of the VAMWNTs, evident in Figures 3b and c, results from capillary forces during the hydrofluoric

² a) S. Huang, L. Dai, A. W. H. Mau, *J. Mater. Chem.* **1999**, 9, 1221.; b) S. Haung, L. Dai, *J. Phys. Chem. B* **1999**, 103, 4223.; c) Y. Yang, S. Haung, H. He, A. W. H. Mau, L. Dai, *J. Am. Soc.* **1999**, 121, 10832.

etching step in the transfer of the VAMWNT film from quartz to gold substrate.

2.2.1. VAMWNT-Au electrodes

The voltage profile characteristics of the VAMWNT-Au electrodes are shown in Figure 4. The voltage of the first discharge half-cycle initially declined over 140 mAh/g with two minor declining voltage plateaus, 1.32 and 0.78 V. This is component X of the irreversible specific capacity (Q_{irr}) and accounted for ~ 12 % of the total first half-cycle specific capacity. It is

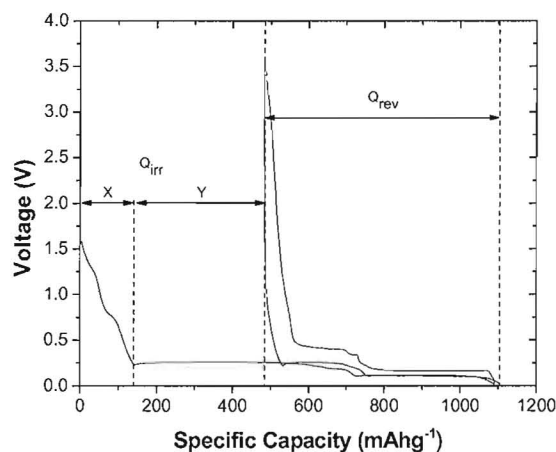


Figure 4 - The first and second discharge cycles of VAMWNT-Au (50 mA/g or 0.1 mA/cm²).

indicative of the irreversible process of solid electrolyte interphase (SEI) layer formation, which consists of insoluble and partially insoluble reduction products of the electrolytes, DEC, EC and LiBF_4 , that form at the surface of the electrodes upon contact with the electrode under load.³ Following the first discharge-charge cycle these voltage plateaus are not present indicating that the formation of the SEI layer is complete. The second component of Q_{irr} , Y, had a

³ a) P. B. Balbuena, Y. Wang, eds., *Lithium-Ion Batteries: Solid-Electrolyte Interphase*. Imperial College Press: London, 2004.; b) D. Aurbach, Y. Ein-Eli, *J. Electrochem. Soc.* **1995**, 142, 1746.; c) A. Naji, J. Ghanbaja, B. Humbert, P. Willmann, D. Billaud, *J. Power Sources* **1996**, 63, 33.

specific capacity of 344 mAh/g (~29 % of total first half-cycle specific capacity) and a relatively constant voltage of 0.26 V. Despite being the first of four voltage plateaus associated with the AuLi reversible alloying process into VAMWNT-Au⁴, this portion of Q_{irr} is mostly likely due to incomplete removal of lithium from AuLi alloy. A reversible specific capacity (Q_{rev}) of 625 mAh/g for the VAMWNT-Au electrodes was obtained with four distinct voltage plateaus (A-D)

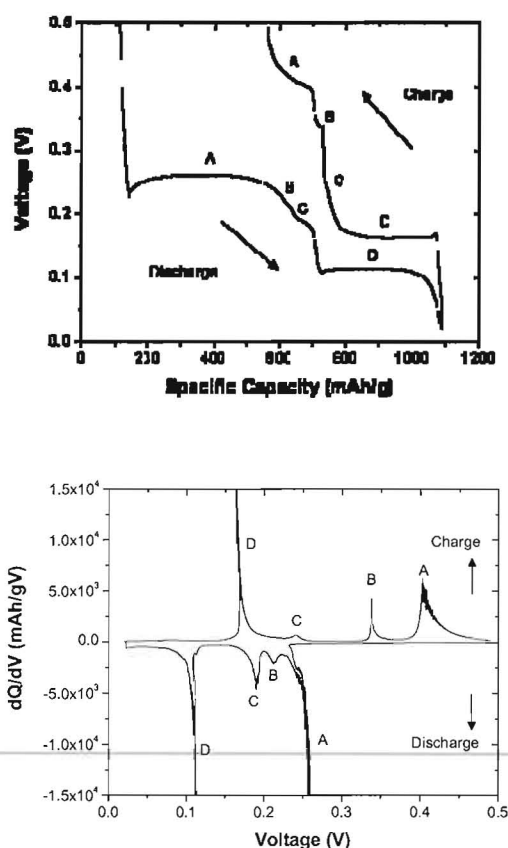


Figure 5 - a) Enlarged spectrum of VAMWNT-Au voltage plateaus and b) differential capacity as a function of voltage for the first discharge and charge half-cycles of VAMWNT-Au.

⁴ G. Taillades, N. Benjelloun, J. Sarradin, M. Ribes, *Solid State Ionics* **2002**, 152-153, 119.

associated with various coexisting phases of AuLi alloy.

A zoomed view of the voltage plateaus and the differential capacity plot of Figure 5 more closely show the electrochemical processes which are occurring. The plateaus and peaks in Figures 5a and 5b, respectively, represent various coexisting phases, of AuLi alloy[4]. During the discharge half-cycle (negative dQ/dV) two major peaks and two minor peaks were observed, which correspond to the two long and two short plateaus in Figure 5a. The two major peaks occurred at 0.26 (A) and 0.11 V (D), where as the minor peaks occurred at 0.21 (B) and 0.19 (C). Similarly, the charge half-cycle (positive dQ/dV) showed two major peaks and two minor peaks at 0.40 (A) and 0.16 V (D) and at 0.34 (B) and 0.24 (C), respectively.

Ex situ electrochemical cycling/X-ray diffraction experiments were utilized to monitor changes in the VAMWNT-Au structure at various points during the electrochemical alloying and de-alloying process. The gold and AuLi X-ray scattering peaks identified in Figure 6 are similar to those seen in literature for the AuLi alloying/de-alloying process [4]. In the pristine sample the VAMWNT 002 spacing is present at $2\theta = 26.24^\circ$ (3.38 Å), as well as, the Au 111 and 220 spacing at $2\theta = 38.50^\circ$ and 44.64° , respectively. The 0.26 V XRD spectra shows a decrease in the Au 111 and 220 spacing peaks and an appearance of peaks associate with AuLi alloy at $2\theta = 31.92^\circ$ and as right shoulders to the Au 111 and 220 spacing peaks. The VAMWNT 002 spacing peak at this voltage was obscured by peaks ($2\theta = 26.99^\circ$ and 27.63°) most likely associated with AuLi alloy structure not yet determined. Spectra taken at the 0.11 V plateau show the disappearance of the Au 111 and 220 and an increase in intensity of the peaks associate with AuLi alloy. In addition, new peaks appeared at $2\theta = 23.81^\circ$, 24.19° , 24.61° , 32.16° , and 32.54° . Complete cell discharge occurred at 0.02 V and the spectra showed minor changes in the AuLi peaks above a 2θ of 38° , while there was an increase in intensity of the $2\theta =$

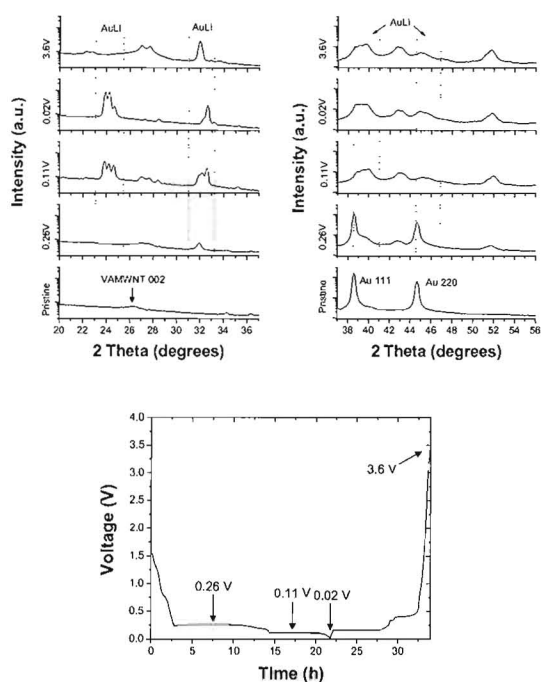


Figure 6 - Ex situ EC/XRD of VAMWNT-Au.

23.81° and 24.19° peaks and a decrease in the $2\theta = 24.61^\circ$ peak. Furthermore, the peak at 31.94° disappeared and the peak at 32.16° reduced in intensity. Finally, a spectrum was taken after a complete discharge and charge of the cell (3.6 V). Here, the AuLi peaks at $2\theta = 23.81^\circ$, 24.19° , 24.61° , 32.16° , and 32.54° completely disappeared leaving only the peak at 31.92° , which was similar to the spectra taken at 0.26 V. Other peaks were present in each of the X-ray diffraction spectra and still need to be identified. It is clear that the XRD data supports the alloying of gold and lithium, however, data to support lithium-ion insertion into the VAMWNTs was inconclusive.

Raman spectroscopy data of VAMWNT-Au discharged to different voltages is shown in Table I and Figure 7. These results indicated that despite the dominance of the Au-Li alloying process in the voltage profile of VAMWNT-Au, lithium-ion insertion into the MWNTs was occurring. Precycled

Table 1. Ex situ Raman spectroscopy data of precycled and cycled VAMWNT-Au.

VAMWNT-Au sample	Peak area ratio (G/G+D)	G Peak (cm^{-1})		D Peak (cm^{-1})	
		Center	Width	Center	Width
Precycled (no Li-Ions)	0.62	1584	45	1354	59
Partial discharge (0.11 V)	0.43	1588	60	1338	90
Full discharge (0.02 V)	0.34	1589	62	1323	119

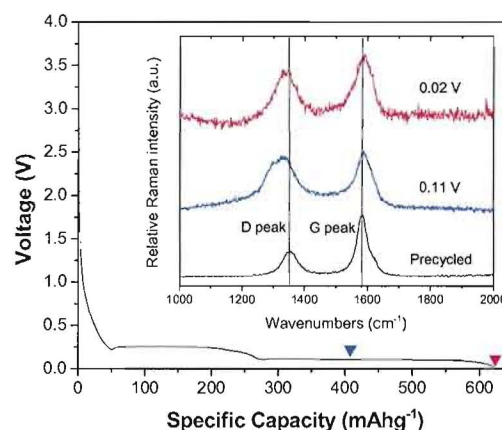


Figure 7 - Ex situ Raman spectra of cycled VAMWNT-Au electrodes.

VAMWNT-Au (no lithium-ions) had prominent features at 1354 cm^{-1} , indicative of the disorder (D) peak usually assigned to the K-point phonons of A_{1g} symmetry typical in polycrystalline graphite and at 1584 cm^{-1} (G peak), which is common in single graphite crystals and is attributed to the zone centered phonons of E_{2g}^2 symmetry. The normalized peak area ratio (A_G/A_G+A_D) for this sample was 0.62. The two other samples were discharged to 0.11 V and 0.02 V. These samples showed a decrease in the normalized peak area ratio indicating an increase in disorder in the MWNT structure as lithium-ion insertion occurred. In addition, a shift in the G to higher wavenumbers and a broadening of the peak occurred, both of which are known graphite behaviors.⁵

⁵ a) J. Panitz, F. Joho, P. Novák, *Applied Spectroscopy* **1999**, 53, 1188.; b) Q. Shi, K. Dokko, D. Scherson, *J. Phys. Chem. B* **2004**, 108, 4789.; c) T. Inaba, H. Yoshida, Z. Ogumi, *J. Electrochem. Soc.* **142**, 1, 20.

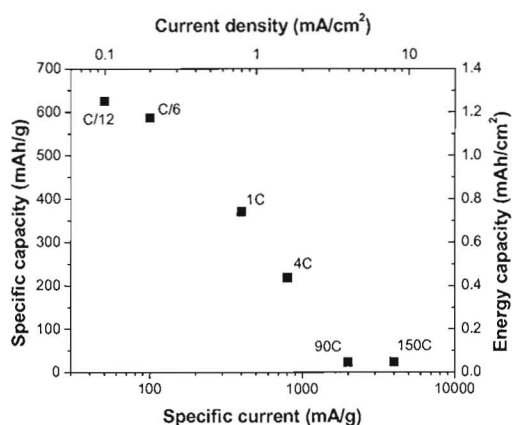


Figure 8 - Capacity as a function of discharge current for VAMWNT-Au electrodes.

Various discharge currents were utilized in order to investigate the rate capability of the VAMWNT-Au. Figure 8 shows the capacity as a function of discharge current. The decline in Q_{rev} as the discharge specific current increased was expected due to larger amounts of stress put on the battery cell at high specific currents and the reduced electrochemical recoverability resultant from rapid discharge rates.⁶ At relatively low discharge specific currents, 50 mA/g (C/12) and 100 mA/g (C/6), Q_{rev} s of 625 and 589 mAh/g, respectively, were obtained. The Q_{rev} s at intermediate discharge specific currents decreased to 371 mAh/g at 400 mA/g (1C) and 219 mAh/g at 800 mA/g (4C). A severe decrease in Q_{rev} was evident at very high discharge specific currents, 2000 mA/g (90C) and 4000 mA/g (150C), yielding Q_{rev} s of 25 and 24 mAh/g, respectively. Coulombic efficiencies of 97.6 % or greater were obtained and after experiencing high discharge currents the VAMWNT-Au had nearly full capacity retention (98 %) when the discharge specific current was decreased to lower values. Furthermore, the majority of discharge specific currents utilized in other studies are typically 100 mA/g or lower, indicating that VAMWNT-Au have

⁶ Linden, D.; Reddy, T.B., *Handbook of Batteries*, 3rd ed. McGraw-Hill Co., Inc.: New York, 2005.

very good rate capability, especially at low and intermediate specific currents.⁷

2.2.2. VAMWNT-Ni electrodes

A very different voltage profile (Figure 9) for the VAMWNT-Ni electrodes was evident due to only the CNTs participation in the electrochemical reaction with lithium as the nickel does not alloy with lithium as gold does. During the first discharge half-cycle two declining voltage plateaus were observed at 1.41 V and 0.77 V which accounted for a Q_{irr} of 938 mAh/g

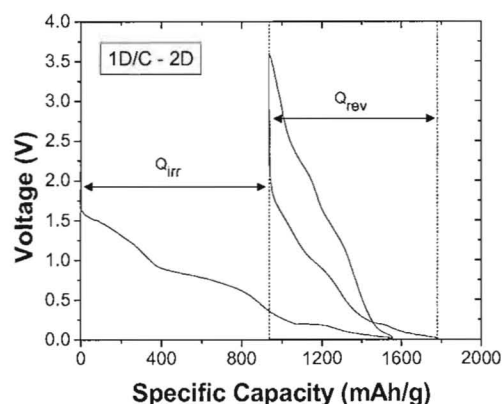


Figure 9 - Voltage profile for the first and second discharge cycle of VAMWNT-Ni (220 mA/g).

and can be attributed entirely to the formation of the SEI layer. Furthermore, the Q_{irr} is ~52 % of the first discharge half-cycle specific capacity, which is fairly high due to the increased surface area of the VAMWNTs. Figure 9 also shows an initial Q_{rev} of 843 mAh/g which then stabilized at approximately 650

⁷ a) G. Maurin, Ch. Bousquet, F. Henn, P. Bernier, R. Almairac, B. Simon, *Chem. Phys. Lett.* **1999**, 312, 14.; b) G. Wu, C. Wang, X. Zhang, H. Yang, Z. Qi, P. He, W. Li, **1999**, 146, 1696.; c) X. Wang, J. Wang, H. Chang, Y. Zhang, *Adv. Funct. Mater.* **2007**, 17, 3613.; d) S. Yang, J. Huo, H. Song, X. Chen, *Electrochim. Acta* **2008**, 53, 2238.; e) Z. Yang, Y. Feng, Z. Li, S. Sang, Y. Zhou, L. Zeng, **2005**, 580, 340.; f) G. Wang, J. Ahn, J. Yao, M. Lindsey, H. Liu, S. Dou, *J. Power Sources* **2003**, 119, 16.

mAh/g by the fifth discharge/charge cycle as seen in Figure 10. Several mechanisms have been suggested to explain the significant increase in Q_{rev} in various types of carbons, including MWNTs, compared to the maximum theoretical Q_{rev} for graphite (372 mAh/g). They include lithium-ion surface adsorption and interactions with hydrogen-containing carbon sites.⁸

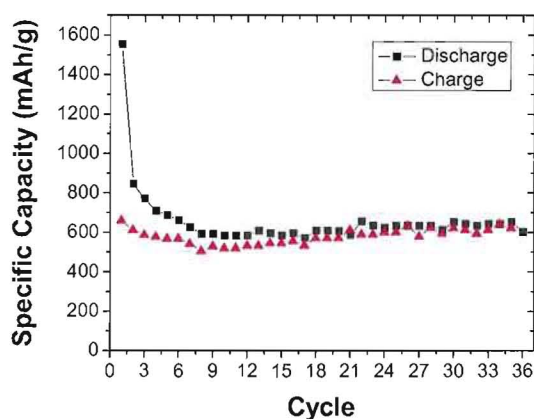


Figure 10 - Specific capacity as a function of cycle for VAMWNT-Ni (220 mA/g).

The voltage plateaus associated with the VAMWNT-Ni reversible electrochemical processes are more easily recognized in Figure 11, which shows the differential capacity as a function of voltage for the second and thirtieth discharge-charge cycles. During the discharge half-cycle (negative dQ/dV) two minor voltage peaks occurred at 0.96 V and 1.61 V, which also occurred during the charge half-cycle (positive dQ/dV) at 1.35 V and 2.32 V. The higher voltage peaks do not appear to be associated with SEI formation, an irreversible process, because they are present during the charge process. Additionally, there is very little change in these voltages from the second

to the thirtieth discharge-charge cycle indicating a stable and reversible electrochemical process. The exact reversible electrochemical process occurring at voltages > 0.90 V is not yet known, but may result from the internal CNT surface adsorption or external CNT surface adsorption, as well as, other mechanisms not known at this time.

A major peak was present during the discharge half-cycle at 0.21 V. This is similar to the 0.21 V plateau

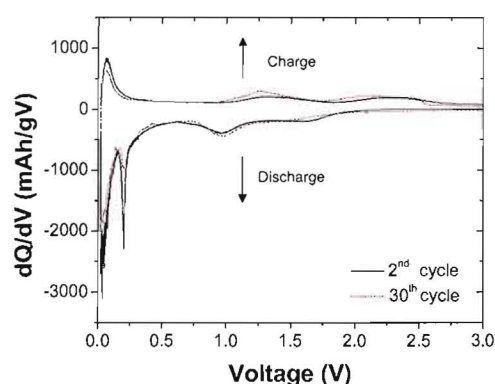


Figure 11 - Differential capacity plot of the 2nd and 30th discharge/charge cycle of VAMWNT-Ni.

seen in the discharge of graphite which corresponds to the transition from a dilute stage 1 phase to a stage 4 phase of lithium-intercalated graphite.⁹ This two-phase transition may be occurring in the graphite-like MWNT; however, further evidence is needed to support this claim. Following the 0.21 V peak there is a gradual decline to the lower cutoff voltage indicating that three or more phases of lithium-MWNT are being present during this segment of the discharge half-cycle. Although the 0.21 V peak is present during the discharge half-cycle it is not present during the charge half-cycle. This implies that the lithium de-insertion and insertion mechanism

⁸ a) J.R. Dahn, T. Zheng, Y. Liu, J.S. Xue, *Science* **1995**, 270, 590. b) P. Papanek, M. Radosavljević, J.E. Fischer. c) J. Eom, H. Kwon, J. Liu, O. Zhou, *Carbon* **2004**, 42, 2589.; d) B. Gao, A. Kleinhammes, X. Tang, C. Bower, L. Fleming, Y. Wu, O. Zhou, *Chem. Phys. Lett* **1999**, 307, 153. e) Z. Yang, H. Wu, *Mater. Chem. Phys.* **2001**, 71, 7.

⁹ a) S. Flandrois, B. Simon, *Carbon* **1999**, 37, 165. b) W. van Schalkwijk, B. Scrosati, eds., *Advances in Lithium-Ion Batteries*. Kluwer Academic/Plenum Publishers: New York, 2002.

differ. Lithium de-insertion may occur in a manner where there are multiple compositions of lithium-MWNT present, as opposed to what is occurring during lithium insertion where a “staged” transition is observed [7].

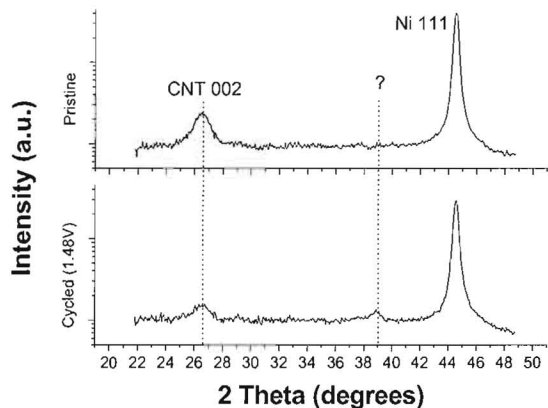


Figure 12 - *Ex situ* EC/XRD data for a pristine and cycled VAMWNT-Ni electrode.

In order to better understand the exact electrochemical processes occurring with the VAMWNTs, *ex situ* X-ray diffraction experiments were conducted (EC/XRD) after the VAMWNT-Ni electrode had been cycled to a specific voltage. Figure 12 shows that once the VAMWNT-Ni electrode has gone through one complete discharge/charge cycle a new peak at $2\theta = 38.9^\circ$ appears, which correlates to a d-spacing of 2.32 Å. Additionally, the CNT 002 peak is also present at $2\theta = 26.4^\circ$ (3.38 Å) in both the pristine and cycled VAMWNT-Ni electrodes. Further *ex situ* EC/XRD are needed to complete this analysis. Scanning electron microscopy and energy dispersive spectroscopy (SEM and EDS) was also taken of a cycled and pristine VAMWNT-Ni electrode. Images (a) and (b) in Figure 13 show a pristine VAMWNT-Ni electrode in which the CNTs are $8.6 \pm 0.3 \mu\text{m}$ in length and the Ni-support layer is $3.5 \pm 0.3 \mu\text{m}$. Image (c) shows a cycled VAMWNT-Ni electrode which has particles of various sizes attached to the exposed end and sides of the CNTs. EDS analysis of these samples

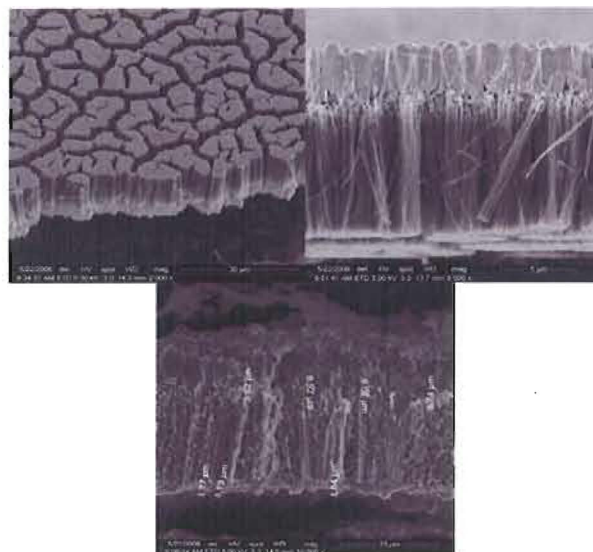


Figure 13 - SEM images of a) pristine VAMWNT-Ni (scale bar = 30 μm), b) side view of pristine VAMWNT-Ni (scale bar = 5 μm), and c) side view of cycled VAMWNT-Ni (scale bar = 10 μm).

(Figure 14) show that the pristine sample (a) is composed of carbon with trace oxygen, while the cycled sample (b) contains carbon, oxygen, and fluorine in high quantities. The increased concentrations of oxygen and fluorine in the cycled sample are evidence of the SEI layer, which is composed of mainly of alkylcarbonates as result of electrolytic degradation of DEC, EC, and LiBF_4 .

To advance our capability of acquiring structural information during the electrochemical processes occurring in the cycling of VAMWNTs, an *in situ* EC/XRD test fixture was fabricated. This test fixture allows for real-time structural data to be obtained while conducting electrochemical cycling experiments. Initial *in situ* experiments are currently being performed and indicated the presence of reversible structural changes as the VAMWNT-Ni/lithium metal cell is cycled. However, more experiments are needed to validate the initial results. In addition to *in situ* electrochemical/X-ray diffraction

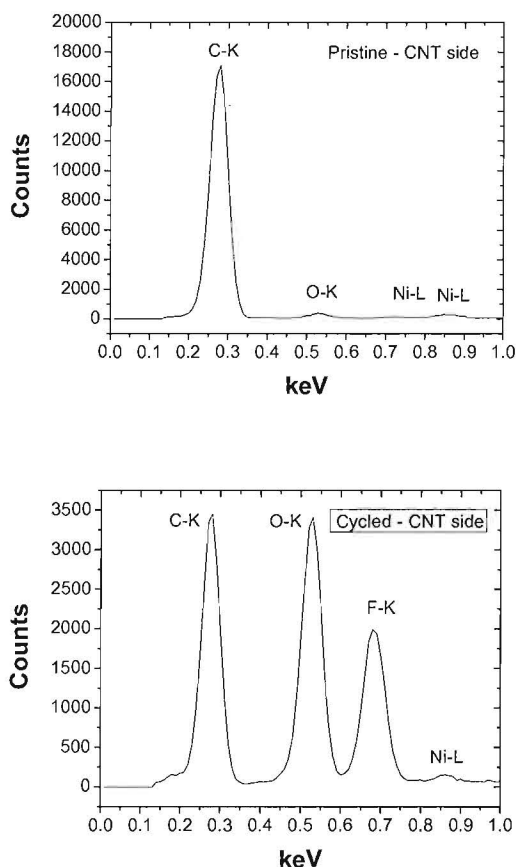


Figure 14 – EDS data for a) pristine and b) cycled VAMWNT-Ni electrode.

capabilities, *in situ* electrochemical/Raman spectroscopy is also being considered. This capability will allow the monitoring of the Raman spectral peaks associated with the ordered and disordered phases of the MWNT while performing electrochemical cycling experiments.

The rate capability of the VAMWNT-Ni electrode was also analyzed by cycling at various currents and is shown in Figure 15. The highest obtained specific capacity was 745 mAh/g (0.195 mA/cm²) when cycling was carried out at 53 mA/g (C/14, 0.013 mA/cm²). The capacity decreased as the current was increased for similar reasons previously noted for the

VAMWNT-Au; however, an excellent specific

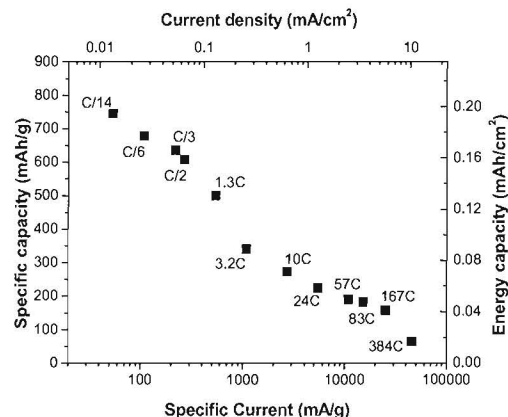


Figure 15 – Capacity as a function of discharge current for VAMWNT-Ni electrodes.

capacity of 500 mAh/g was maintained at moderate discharge rates (1.3C, ~400mA/g, 0.1 mA/cm²). The specific capacity values did not decline below 200 mAh/g until discharge rates exceeded ~20,000 mA/g (~100C, 5 mA/cm²). Not only does the maximum specific capacity value obtained make these electrodes ideal for lithium-ion batteries, but their ability to maintain moderate specific capacity values at high discharge rates make them attractive for applications in which greater energy is needed over shorter periods of time.

2.2.3. Non-aligned MWNT and SWNT

The non-aligned MWNT and SWNT samples were obtained from Nanocomp Technologies Inc. Images of the non-aligned MWNT (a) and SWNT (b) electrodes are shown in Figure 16. The MWNTs had a diameter ranging from 40-60 nm, while the SWNTs are bundles with a diameter ranging from 30-40 nm. Both samples contained small amounts of amorphous carbon, which can also be seen in the SEM images. The voltage profiles of the MWNT and SWNT electrodes were similar to each other, possibly indicating that like lithium-ion insertion mechanisms are occurring (Figure 17). Additionally, their profiles

are similar to those seen in literature for random

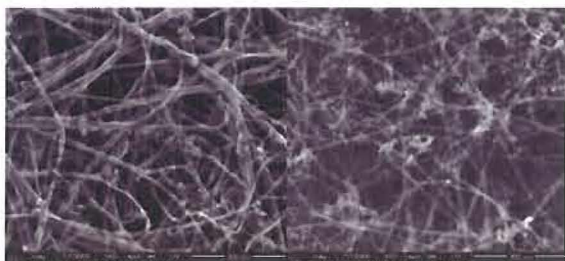


Figure 16 – SEM images of non-aligned (a) MWNTs and (b) SWNTs (scale bar = 500 nm).

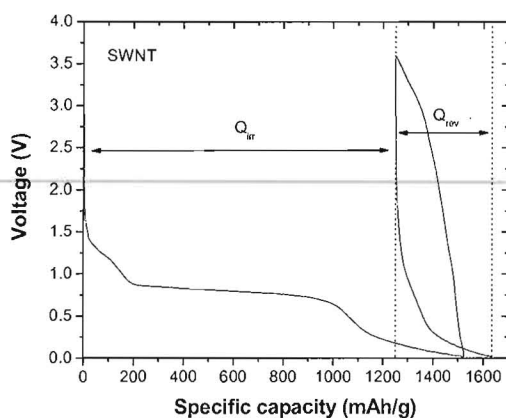
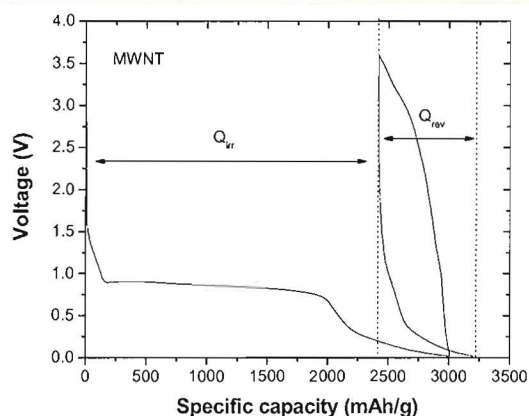


Figure 17 – Voltage profiles for the first and second discharge cycles of non-aligned MWNT and SWNT electrodes.

non-aligned CNT electrodes [7]. Their Q_{irr} values were very different at 2412 mAh/g (MWNT) and 1250 mAh/g (SWNT), but were similar percentages of the first cycle specific capacity, 67 % and 69 %, respectively. Although the Q_{irr} values were significant different, the very large surface area of these samples resulted in their high Q_{irr} , which were mainly composed of SEI layer formations at voltages of 1.25 V and 0.85 V. The Q_{rev} component of the specific capacity consisted of a gradual voltage decline starting around 0.25 V. This would indicate that there is three or more lithium-carbon phases present during the electrochemical lithium insertion/de-insertion from the MWNTs and SWNTs. Additionally, both the MWNT and SWNT electrodes had Q_{rev} values which did not stabilize making it difficult to obtain accurate capacity and rate capability values. This is shown in Figure 18 for the MWNT electrode, which has a first cycle Q_{rev} of 843 mAh/g, but quickly declines to a value of 243 mAh/g at cycle 26 yielding capacity retention of approximately 29 %. This rapid decline in Q_{rev} may result from the non-aligned nature of the MWNT and SWNT electrodes, which allows for lithium-ion to become trapped during the lithium-ion insertion and, subsequently, prevent those lithium-ion from removed during lithium de-insertion, therefore,

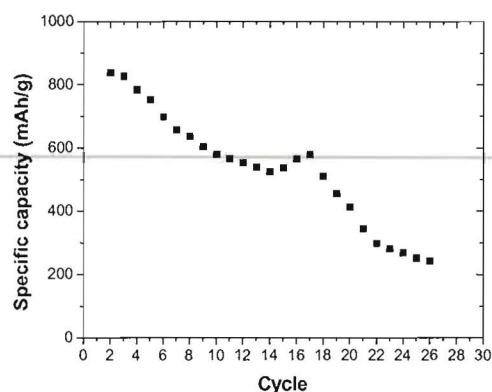


Figure 18 – Capacity as a function of cycle for non-aligned MWNT.

reducing the reversible capacity.

Heat treatment of the MWNT and SWNT electrodes was performed at 200 °C for 2 hours in a hydrogen gas environment prior to electrochemical cycling in order to remove adsorbed water or bound hydroxyl groups from the CNT surface. Raman spectroscopy (Figure 19) showed that the G-D peak area ratio became greater in the heat treated MWNT electrode, which is most likely due to a decrease in the graphitic nature of the MWNT as a result of the heat treatment. The heat treated SWNT electrode did not show any significant change in the G-D peak area ratio. Electrochemical cycling of the heated MWNT and SNWT electrodes has yet to be performed.

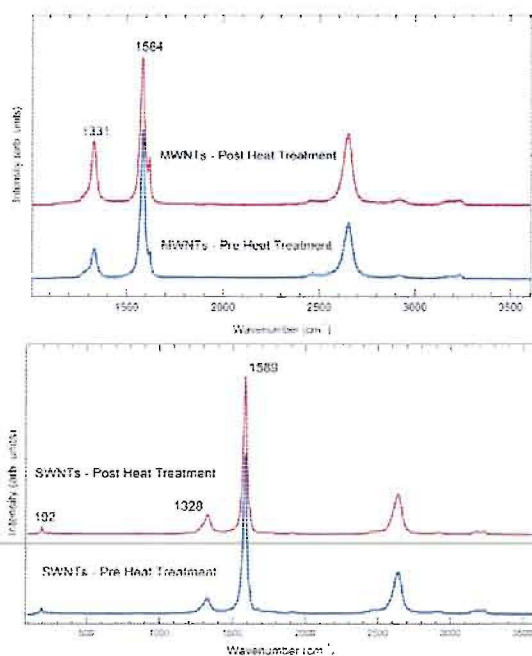


Figure 19 – Raman spectra for the pre- and post-heated non-aligned MWNT and SWNT electrodes.

2.2.4. Poly(p-phenylene benzobisthiazole) (PBZT) conductive polymeric electrodes

The concept of using redox active, conjugated polymeric materials as the active battery electrodes is an area that is gaining momentum due, in part, to the potential of achieving such flexible devices. A fair amount of research has been devoted to the use of oxidatively (p-type) doped conjugated polymers as the positive electrode.¹⁰ Materials such as polyacetylene, polythiophene, polyaniline, and polypyrrole, can have good chemical and environment stability when cycled between their neutral and oxidized form. Reductively (n-type) doped conjugated polymers, however, are typically chemically and environmentally unstable compared to their p-type counterparts making them much less usable as polymer electrodes. Demonstration of a highly flexible, thin film battery comprised of such materials will depend upon the development and use of stable, reductively doped conjugated polymers.

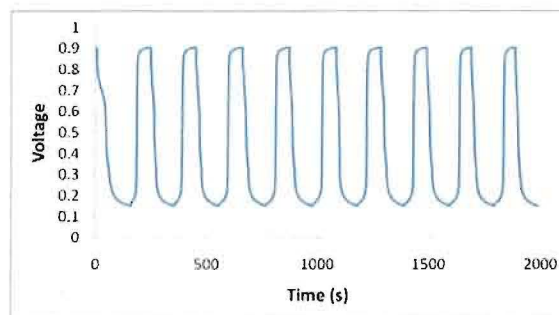


Figure 20 – Cycling voltage profile for PBZT:Nickel metal battery cell.

Recent work has demonstrated poly(p-phenylene benzobisthiazole) (PBZT) to be a stable n-type conjugated polymer. It has been shown that when protonated with various acids to an intermediate level, PBZT acts as a very good electron acceptor, which remarkable can be n-type doped with a variety of even simple metals (Mg, Al, Zn, Fe, Cu) producing

¹⁰ Novák, P. *et al.*, *Chem. Rev.* **1997**, 97, 207.

a highly conductive material. PBZT can also be electrochemically doped - Figure 20 shows the cycling behavior of a gold-metalized PBZT film utilizing concentrated HCl(aq) as the electrolyte and nickel metal as the counter electrode between 0.15 V and 0.90 V. This unique redox behavior makes PBZT an ideal candidate for use as the negative electrode material in a flexible battery configuration. Further research will be required to integrate the PBZT films into complete thin film flexible battery test cells and evaluate their device performance characteristics (storage capacity, rate capability, and cycling behavior). Furthermore, the ability to deposit similar electroactive organic materials onto a nanostructured template (e.g. through electropolymerization of conjugated polymers onto aligned carbon nanotube carpets) and subsequently integrate them into devices will be explored as a means to increase the total internal surface area and thereby improve device performance.

2.2.5. Summary

Employing nanoscale morphologies in battery electrode materials has been seen to greatly improve storage capacity and rate capability, two critical properties needing improvement to keep pace with the ever increasing power requirements of new technologies. However, the ability to control the morphology and to understand how it affects electrochemical behavior is the most critical component in developing new electrode materials which can solve current battery technology limitations, namely those dealing with size and weight. Although, interesting electrochemical and structural data was obtained for the VAMWNTs on a gold support film, they did not allow for exclusive analysis of the electrochemical behavior of the VAMWNTs. Therefore, nickel was used in place of the gold, which provided an approach to isolate the electrochemical behavior of the VAMWNTs. The VAMWNT-Ni electrodes examined in this work showed highly reversible capacities that were almost twice graphite's maximum theoretical capacity. The VAMWNT-Ni also showed excellent rate capability up to currents

not typically utilized in laboratory scale electrode testing. The improvement in these electrochemical properties is thought to be primary a result from the aligned nature of the MWNTs in the direction of battery cell current flow.

In contrast, non-aligned MWNT and SWNT electrodes were examined, which showed poor capacity retention making it difficult to accurately determine rate capability. This poor performance is mostly due to the non-aligned nature of the CNTs. However, both the non-aligned MWNT and SWNT electrodes and the VAMWNT-Ni electrodes need further analysis to determine the various mechanisms of lithium-ion insertion/de-insertion. In addition, the continued development of our *in situ* electrochemical characterization techniques will give us highly detailed data which will aid in determined lithium-ion insertion mechanisms.

3. Fuel Cell Membranes

3.1 Background and Objectives

Polymer electrolyte membrane fuel cells (PEMFCs) function by permitting electrochemical combination of a fuel and an oxidant. These feeds are supplied to the anode (fuel) and cathode (oxidant) in a manner such that power can be continuously drawn from the fuel cell. The feeds can not be allowed to combine and are separated from each other by an electrolyte whose principal function is to permit the transfer of ions through the membrane while prohibiting the direct contact of fuel and oxidant. The polymer membrane is one of the most critical components in the polymer electrolyte fuel cells.

In recent years, PEMFCs have been identified as promising power sources for vehicular transportation and for other applications requiring clean, quiet, and portable power. Hydrogen-powered fuel cells in general have a high power density and are relatively efficient in their conversion of chemical energy to electrical energy. Exhaust from hydrogen-powered fuel cells is free of environmentally undesirable gases

such as nitrogen oxides, carbon monoxide, and residual hydrocarbons that are commonly produced by internal combustion engines. PEMFCs, due to their high efficiency and modularity of design, have the capability to reduce these logistical demands while offering superior War fighter capability and stealthiest. However, the high fuel permeability and limited temperature capability of conventional polymer electrolytes has prevented their operation on highly energy-dense logistic fuels or reformates, which often contain elevated carbon monoxide concentration. Additionally, conventional membrane electrolytes are often based on costly per fluorinated polymers making commercialization economically challenging.

During the past twenty years, ionic polymer ionomers have been the preferred material for this particular application because they are generally easy to process, and permit thin, high volume manufacturing of membrane electrode assemblies (MEAs). Of these materials, DuPont's Nafion has remained the primary system of interest for this application because it is extremely durable, reasonably ionic conducting, and chemically inert¹¹. However, the Nafion polymer system is rather expensive primarily due to the extensive chemistry required for synthesis. Moderate scale production prices of Nafion are projected to be \$600/m² for 100,000m²/year production volumes¹². Additionally, the proton conductivity of Nafion decreases considerably with increasing temperature limiting the performance and fuel tolerance of fuel cell systems. Hydrocarbon polymers containing polar groups that retain high amounts of water over a wide temperature range are particularly attractive and significantly less expensive to synthesize than perfluorinated polymers. Sulfonated high performance polymer systems based on arylene ether, sulfone, and

thioether linkages in the backbone have been synthesized and described in literature^{13,14,15}. These polymer systems are potential candidates for fuel cell applications as they exhibit good thermal and chemical stability and high proton conductivity. In last decade, many researchers have been focused on the synthesis of various sulfonated aromatic polymers that have high thermal, chemical and oxidative stability, good mechanical properties and low cost. Usually they are prepared either by post-sulfonation of commercial polymers or by direct synthesis of sulfonated polymer via copolymerization of sulfonated monomers.

Efforts at the AFRL/RXBN have demonstrated that high molecular weight sulfonated polyarylenethioethersulfone (SPTES)^{16,17} polymers (See Figure 21) exhibit exceptional promise as an electrolyte separator material for fuel cell applications. Highly proton conducting polymers, SPTES, were developed at the Air Force Research Laboratory and were studied for use as the membranes of fuel cell separators. These polymers have been observed to exhibit extremely high conductivity based upon both conventional four

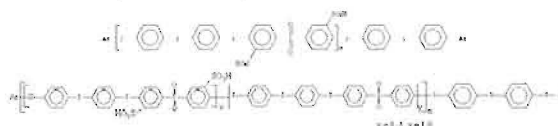


Figure 21 – Structure of sulfonated polyarylenethioethersulfone (SPTES)

¹¹ T. A. Zawodzinski, V. T. Smith, and S. Gottesfeld, *Journal of Electrochemical Society*, **1993**, 140: 1041

¹² P. Dimitrova, K. A. Friedrich, U. Stimming, and B. Vogt, *Solid State Ionics*, **2002**, 150: 115

¹³ M. Ueda, H. Toyota, and T. Teramoto, *J. Polym. Sci. Polym. Chem. Ed.*, **1993**, 31: 853.

¹⁴ R. Nolte, K. Ledjeff, M. Bauer, and R. Mulhaupt, *J. Mem. Sci.*, **1993**, 83: 211.

¹⁵ C. Allam, K. J. Liu, and D. K. Mohanty, *Macromol. Chem. Phys.*, **1999**, 200: 1854.

¹⁶ Z. Bai and T.D. Dang, *Macromol. Rapid Commun.*, **2006**, 27: 1271

¹⁷ Z. Bai, T.D. Dang, and M.F. Durstock, *J. of Membrane Science*, **2006**, 281: 508

probe impedance tests and single cell fuel cell analysis. Additionally, these polymers are strong, chemically inert and thermally stable making them ideal for this application. These polymers have shown extremely high proton conductivity in laboratory screening measurements suggesting a significant improvement over conventional fuel cell electrolytes. Single cell measurements using conventional electrode application techniques have verified that SPTES MEAs are measurably more conductive with better performance, which is superior to Nafion measured using an identical method. Currently, only small quantities of high molecular weight SPTES polymer have been synthesized. However, it is now known that this polymer is relatively easy to cast and has unique hydration capabilities, which suggest that it may be extremely promising as a fuel cell separator. Furthermore, SPTES membranes can be made at a fraction of the cost of the commercial, perfluorinated polymer electrolytes. Although the SPTES polymers show very good potential usages in PEMs, they still have some drawbacks which require additional work. These drawbacks include inadequate mechanical stability and low proton conductivity of the SPTES polymer, which is especially notable when the SPTES polymer has a low amount of sulfonated groups.

Multiblock copolymers are synthesized in order to combine the properties of the constituent homopolymers. Specifically, properties from specific chemical structures are incorporated together to bring multiple property enhancements to the final polymer system. The combination of supramolecular phase separation in multiblock copolymers with self-ordering occurring on a molecular scale can provide interesting properties compared to random copolymers¹⁸. The unique morphology of multiblock copolymers used for PEMs is known to play an important role in determining the membrane's mechanical strength, water uptake, thermal stability,

and proton conductivity¹⁹. It is well known that perfluorosulfonate ionomers have high proton conductivity due to the existence of a "channel-like" network of ions, even at low ion-exchange capacity (IEC)²⁰. Nafion membranes have highly phase-separated hydrophilic and hydrophobic domains, which gives it the necessary performance for fuel cell applications. In the case of sulfonated aromatic polymer membranes, block copolymerization is a potential route to achieve phase-separated morphology²¹. The unsulfonated, hydrophobic phase should enable good mechanical stability and reduce the swelling of the sulfonated blocks, while the hydrophilic sulfonated blocks provide the needed high proton conductivity²².

During Fiscal Year 2007, the first objective was the synthesis and characterization of the multiblock SPTES copolymers containing hydrophilic disulfonated and hydrophobic unsulfonated blocks by a two step polycondensation reaction. The chemical structures are shown in Figure 22. Morphological studies of the multiblock SPTES copolymers show a very well defined phase separation and a distinct morphological architecture (~50nm) compared to random SPTES copolymers, which suggested that the hydrophilic groups aggregate as isolated domains with some local connection of hydrophilic domains as evidenced by the good conductivity of the multiblock SPTES copolymers (See Figure 22). Optimized proton and water transport properties of the polymer membrane and proper water management are crucial for efficient fuel cell operation. While dehydration of the

¹⁸ A.E. Woodward, "Understanding polymer morphology", Hanser Publishers, New York, 1995

¹⁹ Y.S. Yang, Z.Q. Shi, and S. Holdcroft, *Macromolecules* **2004**, 37: 1678,

²⁰ R.A. Weiss, A. Sen, C.L. Willis, and L.A. Pottick, *Macromolecules* **1989**, 22: 4573

²¹ X. Zhang, S.Z. Liu, and J. Yin, *Polymer* **2005**, 46: 1719

²² A. Taeger, C. Vogel, D. Lehmann, and J. Meier-Haack, *React. Funct. Polym.* **2003**, 57: 77

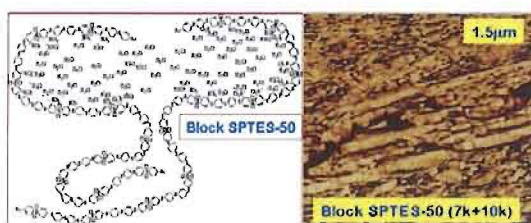


Figure 22 – Chemical structure and AFM images of multiblock SPTES-50 copolymer.

membrane reduces proton conductivity, an excess of water can lead to flooding of the electrodes. Both conditions result in poor fuel cell performance. The proton conductivity of the ionomer membranes relies on the presence of water. At temperatures above 100°C there is a drastic decrease in conductivity of the membrane because of high evaporation rate of water. Thus, a modification of the polymer membranes for operation at higher temperatures would be an alternative approach²³. So by combining optimized water management and proton conductivities into a composite polymer (copolymer or block copolymer), it becomes possible to improve the performance of the PEMs by addressing both of the conductivity issues at the same time. This results in a good balance of properties in the final polymer, and brings a system with potentially superior performance to currently available technologies. Previous research^{24,25}, that focused on the composite approach to prepare the membranes based on proton conducting materials such as sulfonated polyaryleneetheretherketone and SPTES membranes showed excessive swelling, which rendered the membranes brittle upon drying.

²³ S.M. Javaid Zaidi, *Electrochimica Acta* **2005**, 50: 4771

²⁴ J.A. Kerres, A. Ullrich, F. Meier, and Th. Haring, *Solid State Ionics* **1999**, 125: 243

²⁵ Z. Bai, G.E. Price, M. Yoonessi, S.B. Juhl, M.F. Durstock, and T.D. Dang, *J. Membr. Sci.* **2007**, 305, 69

During Fiscal Year 2007, the second objective was the synthesis and characterization of polysiloxane network (PSiN)/SPTES polymer nanocomposites consisting of proton conducting SPTES polymers (SPTES-100) and crosslinkable monomers (DMDMS, TEOS, and DAPMS) by in situ sol-gel processing. The SPTES polymers should confer proton conductivity to the polymer composites, while the siloxane monomers, listed above, will form the network structure in the polymer composites.

3.2 Research Results

To improve the PEM performance and mechanical durability of the SPTES polymers, the aromatic fluorinated, aliphatic fluorinated, and crosslinkable comonomers were introduced to the SPTES polymer backbone by designing the composition to balance polymer hydrophilicity and hydrophobicity. The proper balance should enable good mechanical properties and to reduce the swelling of the sulfonated blocks (which in turn lowers mechanical integrity), and to provide greater proton transport channels in the microstructure, which will enhance proton conductivity of the polymer membranes.

The introduction of aromatic fluorinated segments, higher molecular weight unsulfonated segments, and thermally crosslinkable segments in the polymer backbone can balance the hydrophilicity and hydrophobicity by eliminating the dimensional change during the operation at higher temperature and lower relative humidity. It is anticipated that by incorporating a polymeric block containing one of the above segments into the SPTES polymer, that improved proton transfer mobility will result. This will be achieved because of increasing proton conductivity due to the increased heterogenous morphology which forms proton transfer channels in PEM. The increase of these proton channels potentially will improve the MEA performance, as well as increasing the operational temperature for the entire MEA.

3.2.1. The Crosslinkable Multiblock SPTES-Based Copolymer

The synthesis of a proton exchange membrane (PEM) of the SPTES system by incorporating thermally crosslinkable segment into the polymer backbone can balance the hydrophilicity and hydrophobicity by significantly reducing the dimensional changes during the operation at higher temperature and lower

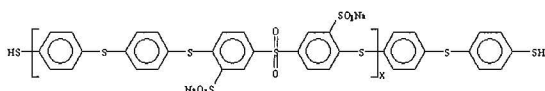


Figure 23 – Chemical structure of difunctional SPTES block (Block A).

relative humidity. Thermally crosslinking polymers were synthesized by following procedure. The polymer block B, (Fluorophenyl diallyl ether, FPAE), which have reactive groups on the end, will be polymerized with difunctional SPTEs polymer (Block A) to obtain proton conducting multiblock copolymers as shown in Figure 23.

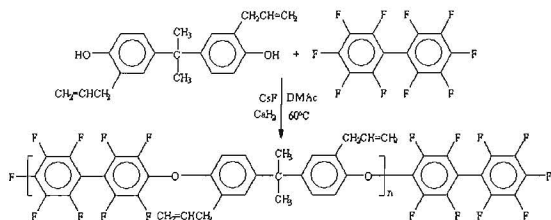


Figure 24 – Synthesis of difunctional crosslinkable FPAE block (Block B).

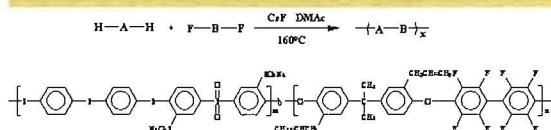


Figure 25 – The reaction scheme of multiblock FPAE-SPTES copolymer.

The reaction scheme of difunctional crosslinkable block (Block B) is shown in Figure 24 while the chemical structures and the reaction scheme of

Table 1 Characteristic of multiblock FPAE-SPTES copolymer and comparison with the multiblock SPTES copolymer, random SPTES copolymer, and Nafion-117

Polymers	Water Uptake (25°C, wt %)	Cal. IEC (meq/g) (IEW, mg/meq)	Proton Conductivity (mS/cm)
Multiblock FPAE-SPTES Copolymer	60	1.82 (550)	185
Multiblock SPTES Copolymer	45	1.82 (550)	256
Random SPTES Copolymer	25	1.82 (550)	100
NaFion-117	19	0.91 (1100)	80

Note: Proton conductivity of the membranes was measured at 65°C, 85% relative humidity.

multiblock FPAE-SPTES copolymer are shown in Figure 25. The properties of multiblock FPAE-SPTES copolymer were listed in Table 1. The multiblock FPAE-SPTES copolymer shows higher water uptake and proton conductivity than Nafion 117 and random SPTES copolymer at the same testing condition. The introduction of thermally crosslinkable segments into the copolymer backbone can be balance the hydrophilicity and hydrophobicity to greatly reduce the dimensional change during the operation at higher temperature and lower relative humidity. The proton conductivity measurements were performed at different temperatures between 45 and 85°C and relative humidities between 35 and 85%. The results of proton conductivity measurements are shown in Figure 26.

Figure 27 shows the TGA curves of multiblock FPAE-SPTES copolymer in its acid and salt forms. The multiblock FPAE-SPTES copolymer exhibited two steps decompositions. The first weight loss was observed around 260°C and is attributed to the splitting-off of sulfonate acid group. The second decomposition step around 490°C corresponds to main chain decomposition. It is clear that the hydrophobic crosslinkable segments should have the influence on the thermal stability of multiblock FPAE-SPTES copolymer comparing with multiblock SPTES copolymer (440°C). Figure 28 shows the T_g (From DMA) is about 250°C, which indicated that the multiblock FPAE-SPTES copolymer can be used up to 250°C.

Mechanical strength of the membrane affects manufacturing conditions of MEAs and durability of PEMFCs. The mechanical properties of the

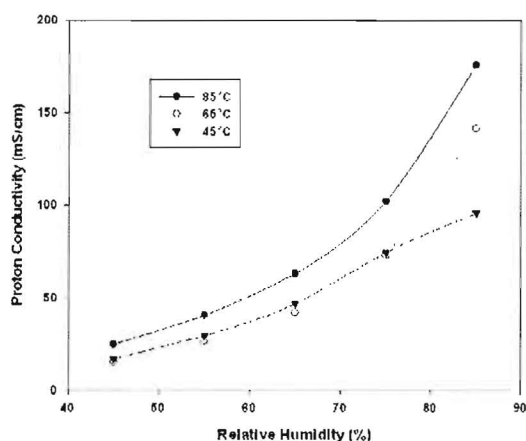


Figure 26 – Temperature and relative humidity dependence of proton conductivity of the multiblock FPAE-SPTES copolymer.

multiblock FPAE-SPTES copolymer membrane, SPTES-50 copolymer membrane, and Nafion-117 membrane were tested with a Tinius Olsen HK10K tensile tester under ambient temperature and at a relative humidity (RH) of 55%; the results of dry films and wet films (hydrated films) are shown in Table 2. From Table 2, we see that the tensile strength of

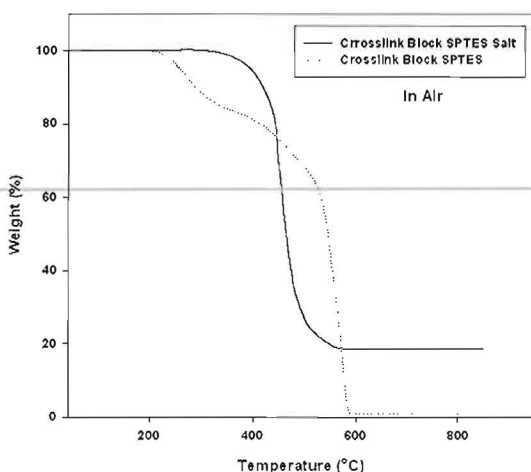


Figure 27 – TGA results of multiblock FPAE-SPTES copolymer (salt form and acid form).

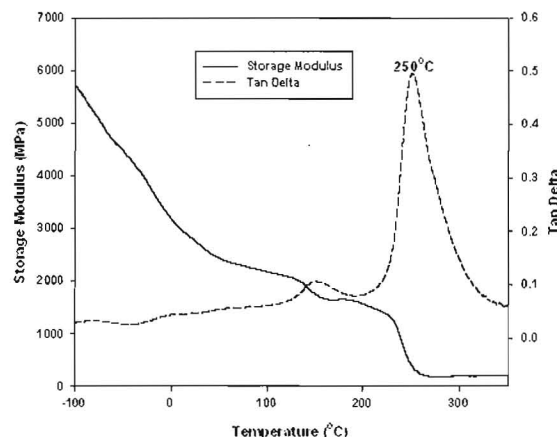


Figure 28 – DMA result of multiblock FPAE-SPTES copolymer.

multiblock FPAE-SPTES copolymer membrane (dry film) is (22.4MPa) is comparable to SPTES-50 copolymer (34.6MPa) and Nafion-117 (31.4MPa). Young's modulus for the membranes of multiblock FPAE-SPTES copolymer and SPTES-50 copolymer are 1.02 and 1.23GPa, respectively; these values are much higher than the measured tensile modulus of Nafion-117 (0.357GPa). It follows from Table 2 that multiblock FPAE-SPTES copolymer membrane shows elongation at break of 13.6%, this elongation is much lower than that of SPTES-50 copolymer (31.6%) and Nafion-117 (270%), which clearly indicates good toughness of multiblock FPAE-SPTES copolymer membranes at 55% relative humidity. It is worth mentioning that the tensile strength (9.37MPa) and tensile modulus (0.402GPa) of wet multiblock FPAE-SPTES copolymer membrane are much lower than SPTES-50 copolymer (33.0MPa, 0.987GPa); the wet membrane also exhibits a higher elongation at break (19.1%) compared to the membrane in the dry state (13.4%), but it is much superior to Nafion-117. It has been demonstrated that hydration improves the plasticity of the multiblock FPAE-SPTES copolymer. On other hand, multiblock FPAE-SPTES copolymer membrane is also considerably stiffer than Nafion as reflected by the larger tensile modulus values.

Table 2 Mechanical properties of multiblock FPAE-SPTES copolymer membranes

Polymers	Tensile Strength (MPa)	Tensile Modulus (GPa)	Elongation (%)
FPAE-SPTES Copolymer (Dry)	22.4	1.02	13.4
FPAE-SPTES Copolymer (Wet)	9.37	0.402	19.1
* Random SPTES-50 (Dry)	34.6	1.23	31.6
* Random SPTES-50 (Wet)	33.0	0.987	86.6
* Nafion-117 (Dry)	31.4	0.357	270
* Nafion-117 (Wet)	19.8	0.152	201

*For comparison with FPAE-SPTES samples

3.2.2. Aromatic Fluorinated Multiblock SPTES Copolymer (Multiblock AFB-SPTES Copolymer)

The synthesis of the SPTES-based copolymer with an aromatic fluorinated segment incorporated into the polymer backbone can balance the hydrophilicity and hydrophobicity to eliminate the dimensional change during the operation at higher temperature and lower relative humidity. The aromatic fluorinated segment was introduced into the SPTES-based material by in-situ copolymerization. The synthesis procedure and the chemical structure of aromatic fluorinated block (AFB) are shown in Figure 29, while the chemical structure and reaction scheme of multiblock AFB-SPTES copolymer are presented in Figure 30.

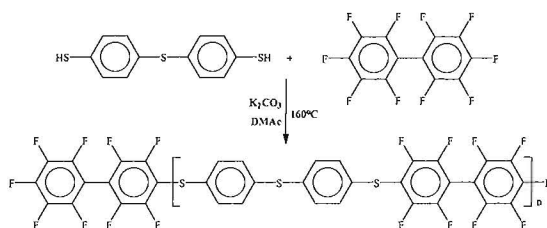


Figure 29 – Synthesis scheme of AFB (Block B).

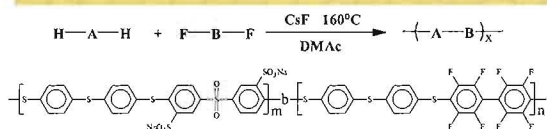


Figure 30 – Synthesis scheme of multiblock AFB-SPTES copolymer.

The characterization of multiblock AFB-SPTES copolymer was done by GPC, which confirmed the molecular weight of the synthesized copolymers. The

Table 3 Water uptake and GPC results of the multiblock AFB-SPTES copolymer

Polymers	Water Uptake (25°C, wt %)	MW of Block A (Calculation)	MW of Block B (Calculation)	Mn (GPC)	PDI (GPC)
Multiblock SPTES-50 Copolymer	45	9.0k	6.5k	22.9k	2.23
Multiblock AFB-SPTES Copolymer	39	5.0k	6.6k	17.3k	3.65

Table 4 TGA results of multiblock AFB-SPTES copolymer (Salt form)

AFB-SPTES Copolymer	T _{el} , °C at 5 % Wt loss	T _{el} , °C at 20 % Wt loss	T _{el} , °C at 40 % Wt loss	Residue (wt%)
In Air	420	--	--	12
In N ₂	430	510	720	55

results of GPC measurements are shown in Table 3. The characterization of multiblock AFB-SPTES copolymer was done by TGA, which confirms the thermal stability of the copolymers. The results of TGA measurement were shown in Table 4. TGA of the multiblock AFB-SPTES copolymer containing sodium cations in air showed a single step decomposition around 420°C, with a residue measured (12wt%) due to the Na in the polymer side chain (residue likely sodium oxide). The TGA of multiblock AFB-SPTES copolymer in N₂ exhibited a three step degradation pattern. The first weight loss

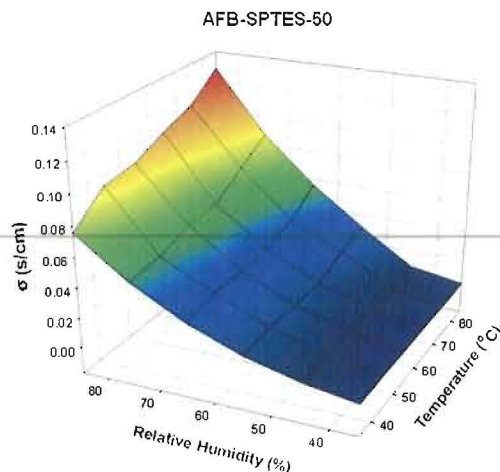
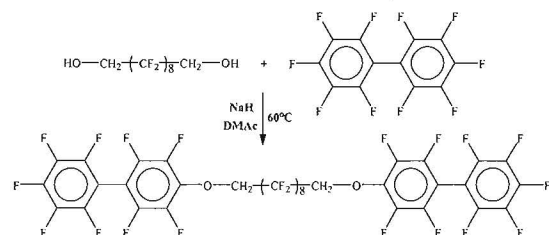


Figure 31 – Proton conductivity of multiblock AFB-SPTES-50 at different temperatures and different relative humidities.

(5wt%) was observed around 430°C; the second decomposition step around 510°C (20%) corresponds to the main chain decomposition, and the observed third weight loss (>40%) was around 720°C which likely corresponds to carbon char undergoing additional pyrolysis and thermal decomposition. The final residual was about 55 wt%. The characterization of proton conductivity of multiblock AFB-SPTES copolymers for the temperature range of 35°C to 85°C and relative humidity of 35% to 85% is shown in Figure 31 for multiblock AFB-SPTES-50, a copolymer containing 50 mole% sulfonate content in copolymer backbone.

3.2.3. Flexible Fluorinated Block SPTES-Based Copolymers

As with the incorporation of aromatic fluorinated blocks and cross-linkable blocks to improve the durability, dimensional stability, and mechanical integrity of the PEM, a flexible segment was introduced into SPTES polymer to determine how it would affect PEM performance. Further, by incorporating a flexible block into the SPTES, improved proton mobility (proton conductivity) will result due to the greater heterogenous morphology and increased formation of proton transfer channels in PEM. Based on this point, the multiblock SPTES-based copolymer was synthesized with specific goals for molecular weight, flexibility and dimensional stability. The synthesis procedure and structures of the flexible fluorinated polymer (FFP) block are presented in Figure 32, while the synthesis reaction



scheme and chemical structures of multiblock FFP-

Figure 32 – Synthesis scheme of FFP block (Block B).

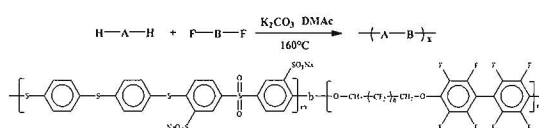


Figure 33 – Synthesis of multiblock FFP-SPTES copolymer.

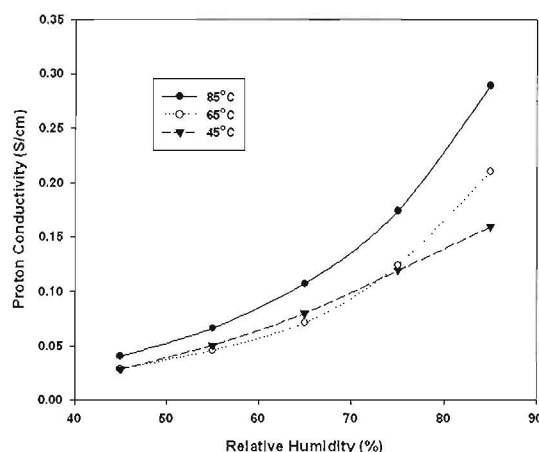


Figure 34 – Proton conductivity of multiblock FFP-SPTES copolymer at different temperatures and different relative humidities.

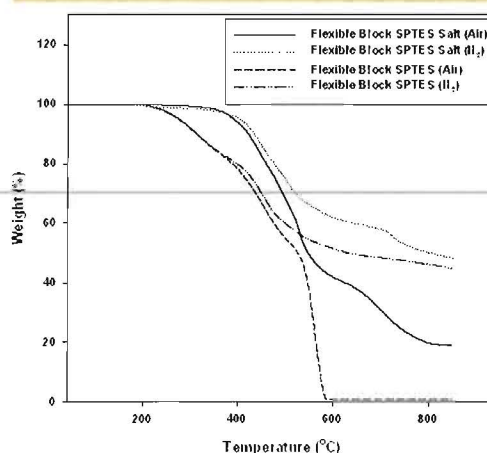


Figure 35 – TGA results of multiblock FFP-SPTES copolymer Salt form and Acid from both in Air and N₂.

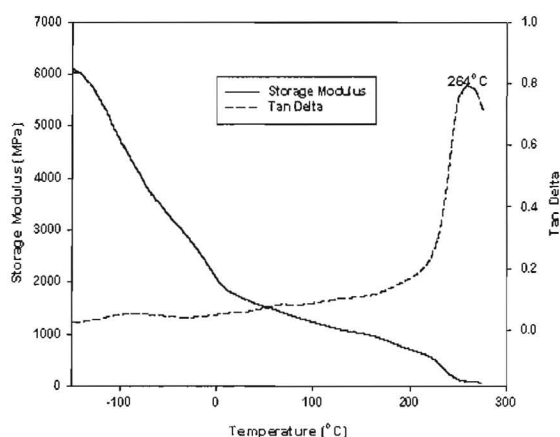


Figure 36 – DMA results of multiblock FFP-SPTES copolymer.

SPTES copolymer are shown in Figure 33.

The proton conductivity was measured at 45°C, 65°C, and 85°C under various relative humidity conditions and the result is plotted in Figure 34. It is evident from Table 1 that the multiblock FFP-SPTES copolymer has much higher proton conductivity than random SPTES-50 polymer. Figure 35 shows TGA results of multiblock FFP-SPTES copolymer and its salt form in air and N₂. The salt form of the copolymers shows a single step degradation around 420°C in both air and N₂, leaving behind some inorganic residue. The multiblock FFP-SPTES copolymer exhibited a two step degradation pattern in air and in N₂. The first weight loss was observed around 270°C. It is attributed to the splitting-off of sulfonic acid group. The second degradation step around 410°C corresponds to the main chain decomposition. Figure 36 presents the T_g results from the peaks of the DMA loss tangents. The T_g values obtained from DMA are 264°C, which indicates that the polymer can be used up to 260°C with good thermal stability making this material suitable for high temperature uses.

Table 5 shows the mechanical properties of multiblock FFP-SPTES copolymer membrane under

Table 5 Mechanical properties of multiblock FFP-SPTES copolymer membranes compared to SPTES-50 copolymer and Nafion-117

Polymers	Tensile Strength (MPa)	Tensile Modulus (GPa)	Elongation (%)
FFP-SPTES Copolymer (Dry)	23.0	0.827	4.4
FFP-SPTES Copolymer (Wet)	3.74	0.142	7.0
* Random SPTES-50 (Dry)	34.6	1.23	31.6
* Random SPTES-50 (Wet)	33.0	0.987	86.6
* Nafion-117 (Dry)	31.4	0.357	270
* Nafion-117 (Wet)	19.8	0.152	201

*For comparison with FFP-SPTES samples

dry and wet conditions as well as the values for SPTES-50 copolymer and Nafion-117 membranes. In the dry film test, multiblock FFP-SPTES copolymer membrane exhibited greater modulus than Nafion-117. It is worth mentioning that the tensile strength of the multiblock FFP-SPTES copolymer membrane, the SPTES-50 copolymer membrane, and the Nafion-117 membrane is in comparable ranges. Elongation of the multiblock FFP-SPTES copolymer membrane is much lower than the SPTES-50 copolymer and Nafion-117. In the wet film test, the maximum strength of the wet multiblock FFP-SPTES copolymer membrane (3.74MPa) is much lower than that of the SPTES-50 copolymer membrane (33.0MPa) and Nafion-117 membrane (19.8MPa). The modulus of multiblock FFP-SPTES copolymer membrane is much lower than the SPTES-50 copolymer; however, it has the same modulus with Nafion-117. Upon hydration, multiblock FFP-SPTES copolymer was found to lose a large proportion of its strength, believed to be due to the introduction of flexible fluorinated block in the copolymer backbone. On the other hand, wet multiblock FFP-SPTES copolymer membrane also exhibits a higher elongation at break (7.0%) compared to the membrane in the dry state (4.4%). It is demonstrated that hydration improves the plasticity of the multiblock FFP-SPTES copolymer.

3.2.4. Performance and Morphology of Polysiloxane network/SPTES Nanocomposites

Figure 37 shows the temperature dependence of water uptake of Polysiloxane network/SPTES polymers (PSiN/SPTES-100) nanocomposites. The

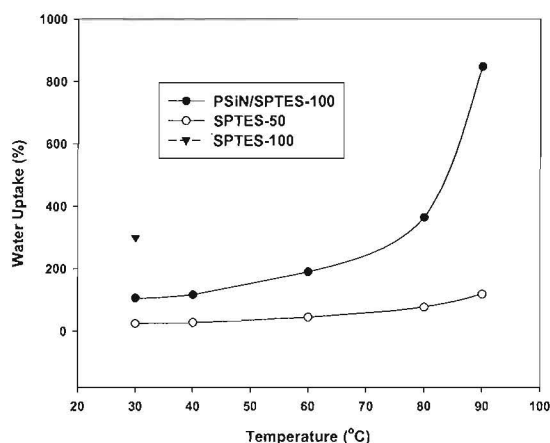


Figure 37 – Water uptakes of SPTES-100 polymers, SPTES-50 copolymer, and PSiN/SPTES-100 nanocomposites as a function of the temperature.

SPTES-100 polymer can only be tested at room temperature for the water uptake; while the PSiN/SPTES-100 nanocomposites are determined up to 90°C, the behaviors are compatible to SPTES-50 copolymer. The water uptake of PSiN/SPTES-100 nanocomposite was reduced by 200% after blending with 5wt% siloxane-network.

Figure 38 shows the proton conductivities of PSiN/SPTES-100 nanocomposite as the temperature increased at 85wt% relative humidity. The proton conductivity of PSiN/SPTES-100 nanocomposite (168mS/cm) was lower than SPTES-100 polymer (300mS/cm) at 65°C, 85wt% relative humidity, which is the highest temperature for the test of the proton conductivity of SPTES-100 polymer. While PSiN/SPTES-100 nanocomposite can go to 85°C or higher for the test of proton conductivity. The straight lines show Arrhenius behavior with comparable activation energies for the two SPTES samples which are higher than the activation energy for Nafion-117.

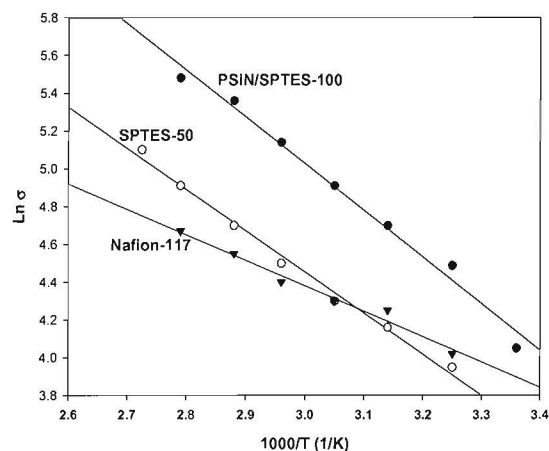


Figure 38 – The proton conductivity of PSiN/SPTES-100 nanocomposites as a function of the inverse temperature comparing with SPTES-50 copolymer and Nafion-117.

SEM images are shown in Figure 39 (A). PSiN particles are observed as darker areas on SEM and are uniformly embedded throughout the membrane matrix, which is quite different from the features observed in nanocomposite membranes where the nanoparticles are physically mixed with proton-conducting polymer solution for membrane formation. The interpenetrating network of the PSiN and SPTES-100 matrix, obtained in the present investigation, could not be obtained by a simple mixing of nano SiO₂ with SPTES-100 solution. The PSiN particles are hardly visible in the PSiN/SPTES nanocomposite membrane at this level of magnification though they are uniformly distributed throughout the matrix. The domain size of the inorganic phase is from 500nm to 1.0μm, which is evident from the SEM micrographs at higher magnification. Figure 39 (B) shows SEM micrographs of PSiN/SPTES nanocomposite membrane after being hydrated. PSiN domain size for the PSiN/SPTES nanocomposite membrane was ~1.0μm. Uniform distribution of PSiN particles of varying size and round shape could be observed together. Even though these initial attempts have not produced a

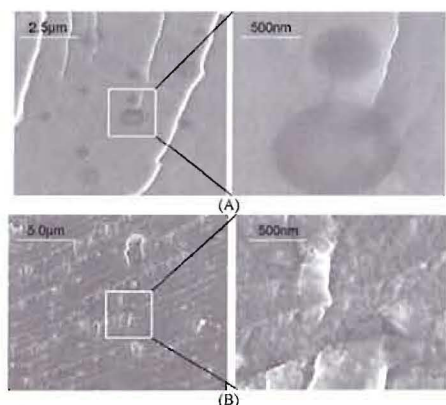


Figure 39 – SEM images of PSiN/SPTES-100 nanocomposite membrane: (A) Dry film observation, (B) Wet film observation.

true nanocomposite membrane with nanometer-scale particle dimensions, the observed morphological features are very promising.

Embedded PSiN particles may impart thermal and mechanical stability to the membrane matrix, apart from close interactions with sulfonic acid functional groups in the polymer chain. Uniform distribution of PSiN particles in the whole matrix is the ideal situation to establish continuous conduction pathways in all directions with minimum baffling of SPTES-100 conduction channels. Based on the SEM morphological features, we would expect the nanocomposite membranes to have vastly improved properties in comparison with pristine polymer. The observed SEM morphology is highly amenable to the formation of continuous conduction pathways by the SPTES-100 through the siloxane network.

Figure 40 shows the polarization curves of PSiN/SPTES-100 nanocomposite, SPTES-50 copolymer and Nafion-117 MEAs, providing a comparison of the relative performances of the three systems. The overall electrochemical performance of PSiN/SPTES-100 nanocomposite membrane MEA using conventional electrode inks with perfluorinated binders was lower than that of SPTES-50 copolymer and Nafion-115 MEA under comparable conditions

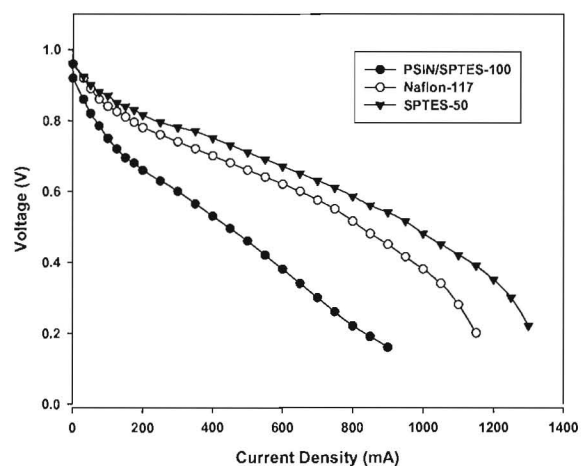


Figure 40 – MEA performance comparisons of PSiN/SPTES nanocomposite, SPTES-50 copolymer, and Nafion-115.

(80°C, 55wt% relative humidity, 1atm, stoichiometry = 2 for H₂ and Air). A higher current density of 820mA/cm² was obtained for the SPTES-50 copolymer membrane-based MEA as compared to a current density of 360mA/cm² for PSiN/SPTES nanocomposite membrane-based MEA and a current density of 640mA/cm² for Nafion-117 membrane-based MEA at 0.6 V potential. Estimates of hydrogen fuel permeability based upon measured open circuit voltage (OCV) indicate that SPTES-50 copolymer MEA (OCV=0.96V) and Nafion-117 MEA (OCV=0.95V) exhibit similar rates of fuel cross-over, while PSiN/SPTES nanocomposite MEA (OCV=0.91V) is much higher rate of fuel cross-over.